A COMPUTATIONAL ANALYSIS OF DETONATION OF BURIED MINES

M. Grujicic[1*], B. Pandurangan[1] and B. A. Cheeseman[2]

[1] *Department of Mechanical Engineering Clemson University, Clemson SC 29634-0921*
[2]*Army Research Laboratory – Survivability Materials Branch Aberdeen, Proving Ground, MD 21005-5069*

Abstract—A nonlinear-dynamics transient computational analysis of the explosion phenomena associated with detonation of 100g of C4 high-energy explosive buried at different depths in sand is carried out using the AUTODYN computer program. The results obtained are compared with the corresponding experimental results obtained in Ref. [1]. To validate the computational procedure and the materials constitutive models used in the present work, a number of detonation-related phenomena such as the temporal evolutions of the shape and size of the over-burden sand bubbles and of the detonation-products gas clouds, the temporal evolutions of the side-on pressures in the sand and in air, etc. are determined and compared with their experimental counterparts. The results obtained suggest that the agreement between the computational and the experimental results is reasonable at short post-detonation times. At longer post-detonation times, on the other hand, the agreement is less satisfactory primarily with respect to the size and shape of the sand crater, i.e. with respect to the volume of the sand ejected during explosion. It is argued that the observed discrepancy is, at least partly, the result of an inadequacy of the generic materials constitutive model for the sand which does not explicitly include the important effects of the sand particle size and the particle size distribution, as well as the effects of moisture-level controlled inter-particle friction and cohesion. It is further shown that by a relatively small adjustment of the present materials model for sand to include the potential effect of moisture on inter-particle friction can yield a significantly improved agreement between the computed and the experimentally determined sand crater shapes and sizes.

NOMENCLATURE

A	-	Constant in JWL Equation of State
B	-	Constant in JWL Equation of State
E	-	Internal energy
G	-	Shear modulus
?	-	Constant-pressure to constant-volume specific heats ratio
?	-	Gruneisen parameter
P	-	Pressure

---

[*] E-mail: mica.grujicic@ces.clemson.edu
 Tel: (864) 656-5639, Fax: (864) 656-4435

Report Documentation Page		*Form Approved* *OMB No. 0704-0188*

Public reporting burden for the collection of information is estimated to average 1 hour per response, including the time for reviewing instructions, searching existing data sources, gathering and maintaining the data needed, and completing and reviewing the collection of information. Send comments regarding this burden estimate or any other aspect of this collection of information, including suggestions for reducing this burden, to Washington Headquarters Services, Directorate for Information Operations and Reports, 1215 Jefferson Davis Highway, Suite 1204, Arlington VA 22202-4302. Respondents should be aware that notwithstanding any other provision of law, no person shall be subject to a penalty for failing to comply with a collection of information if it does not display a currently valid OMB control number.

1. REPORT DATE **2006**	2. REPORT TYPE	3. DATES COVERED **00-00-2006 to 00-00-2006**
4. TITLE AND SUBTITLE **A Computationa Analysis of Detonation of Buried Mines**		5a. CONTRACT NUMBER
		5b. GRANT NUMBER
		5c. PROGRAM ELEMENT NUMBER
6. AUTHOR(S)		5d. PROJECT NUMBER
		5e. TASK NUMBER
		5f. WORK UNIT NUMBER
7. PERFORMING ORGANIZATION NAME(S) AND ADDRESS(ES) **Celmson University,Department of Mechanical Engineering,Clemson,SC,29634**		8. PERFORMING ORGANIZATION REPORT NUMBER
9. SPONSORING/MONITORING AGENCY NAME(S) AND ADDRESS(ES)		10. SPONSOR/MONITOR'S ACRONYM(S)
		11. SPONSOR/MONITOR'S REPORT NUMBER(S)

12. DISTRIBUTION/AVAILABILITY STATEMENT
Approved for public release; distribution unlimited

13. SUPPLEMENTARY NOTES
Multidiscipline Modeling in Materials and Structures, 2, pp. 363-387, 2006

14. ABSTRACT

A nonlinear-dynamics transient computational analysis of the explosion phenomena associated with detonation of 100g of C4 high-energy explosive buried at different depths in sand is carried out using the AUTODYN computer program. The results obtained are compared with the corresponding experimental results obtained in Ref. [1]. To validate the computational procedure and the materials constitutive models used in the present work, a number of detonation-related phenomena such as the temporal evolutions of the shape and size of the over-burden sand bubbles and of the detonation-products gas clouds, the temporal evolutions of the side-on pressures in the sand and in air etc. are determined and compared with their experimental counterparts. The results obtained suggest that the agreement between the computational and the experimental results is reasonable at short postdetonation times. At longer post-detonation times, on the other hand, the agreement is less satisfactory primarily with respect to the size and shape of the sand crater, i.e. with respect to the volume of the sand ejected during explosion. It is argued that the observed discrepancy is, at least partly, the result of an inadequacy of the generic materials constitutive model for the sand which does not explicitly include the important effects of the sand particle size and the particle size distribution, as well as the effects of moisture-level controlled inter-particle friction and cohesion. It is further shown that by a relatively small adjustment of the present materials model for sand to include the potential effect of moisture on inter-particle friction can yield a significantly improved agreement between the computed and the experimentally determined sand crater shapes and sizes .

15. SUBJECT TERMS

16. SECURITY CLASSIFICATION OF:			17. LIMITATION OF ABSTRACT	18. NUMBER OF PAGES	19a. NAME OF RESPONSIBLE PERSON
a. REPORT **unclassified**	b. ABSTRACT **unclassified**	c. THIS PAGE **unclassified**	**Same as Report (SAR)**	**26**	

R_1	-	Constant in JWL Equation of State
R_2	-	Constant in JWL Equation of State
?	-	Density
v	-	Specific volume
w	-	Constant in JWL Equation of State
x	-	Spatial coordinate
y	-	Spatial coordinate
Y	-	Yield stress

Subscripts

| o | - | Initial condition |

1. INTRODUCTION

Detonation of high-energy explosives and the subsequent interaction of the detonation products and the associated shock waves with the surrounding media and structures involve highly non-linear phenomena of a transient nature. In order to maximize the destructive effects of the explosion or to devise means/strategies for minimizing such effects, a large range of diverse physical phenomena must be considered. While, in principle, one would prefer to study the aforementioned detonation phenomena using an analytical technique, in hope of elucidating the underlying physics of the problem, analytical methods typically entail major simplifying assumptions so that their predictions are often questionable or even contradicted by the experimental observations [1]. Consequently, a better understanding of the explosion phenomena is being gradually gained by combining physical experiments with numerical modeling techniques [2-4]. This approach is utilized in the present work in which the experimental results pertaining to the explosion of a 100g shallow-buried C4 high-energy explosive reported in Ref. [1] are compared with a detailed numerical modeling of the same physical problem using AUTODYN, a state of the art non-linear dynamics simulation software [2].

2. PROBLEM DEFINITION AND COMPUTATIONAL ANALYSIS

2.1. Soil Response Following Explosion of Shallow-buried Mines

While an explosion is a continuous event taking place over a relatively short period of time (typically over several hundred microseconds), its analysis is often divided into three distinct phases: (i) the initial phase dominated by the detonation of the explosive and by the interactions between the resulting gaseous detonation products and the soil surrounding the buried explosive; (ii) the second phase associated with a substantial expansion of the detonation products, initial ejection of the soil and with the formation and propagation of an air shock and (iii) the last stage of an explosion which is dominated by a substantial ejection of the soil. In the remainder of this section, a more detailed description is given of each of the three stages of an explosion.

When the explosion of a mine is initiated, detonation waves begin to propagate from the points of initiation of the explosion, transforming an (typically solid) explosive into a mass of hot, high-pressure gaseous detonation products. The interactions of the high-pressure detonation products with the surrounding soil result in different responses of different portions of the soil, depending (primarily) on their distance from the explosive and on their physico-mechanical properties. The initial stage of explosion plays an important role in the overall effectiveness and lethality of a buried mine since it controls the amount of explosive energy available to impact the target structure/personnel. Many parameters influence the amount of energy absorbed by the soil, and among these parameters the most important ones are found to be the depth of burial, soil physical and mechanical properties and the moisture content of the soil [1, 3, and 5]. The optimal depth of burial for shallow buried explosives corresponds to a condition under which the charge explosion is followed by apreferential venting of the detonation products and soil ejection in the upward direction while the amount of the explosion energy absorbed by the (un-ejected) soil is minimized. Larger density and larger moisture contents generally give rise to an increase in the soil's ability to transmit shock and reduce soil's ability to absorb energy.

When the compressive stress wave, which is initiated at the detonation products/soil interface and travels through the soil, reaches the soil/air interface (the second stage of explosion), it partially reflects from the interface back into the soil as a tensile stress wave and partially becomes transmitted to the air as a shock wave. The tensile stresses give rise to the expansion of the soil to help sustain the air shock. Ultimately, however, the tensile stresses cause fragmentation of the soil which, under the influence of the high-pressure detonation products, becomes ejected upward creating a cavity in the ground. This subsequently causes a complex system of shock and rarefaction waves to be established within the gaseous detonation products residing in the cavity. This is accompanied by a rapid adiabatic expansion of these gases which gives rise to the formation of additional air shock waves that carry a significant amount of energy to be transferred to the target.

The amount of soil ejected in the second phase of explosion, which lasts typically only few microseconds, is relatively small. Consequently, in the second stage of explosion, the majority of the explosion energy transmitted to the target is associated with the air shock waves. In the third stage of explosion, complex interactions between the compression waves and the rarefaction waves in the detonation products and the soil within the cavity continue to take place and erode the surrounding soil and eject it, at a high speed, in the upward direction. Consequently, within this stage of explosion, which can sometimes last for few hundreds of milliseconds, a substantial volume/mass of the soil is ejected. The ejected soil is responsible for the majority of the explosion energy transferred to the target in this stage of explosion. The trajectory of the ejected soil particles/fragments is generally in an upward direction and confined within an inverted cone region with an included angle between 60 and 90 degrees. Typically the included angle decreases with a decrease in the depth of burial and a decrease in the soil density, which can be easily rationalized, since these two conditions promote the straight upward ejection of the detonation products and the soil [1].

2.2. Problem Definition

The problem analyzed computationally in the present study is identical to the one

investigated experimentally in Ref. [1]. A schematic of the problem is shown in Fig. 1. The problem can be briefly described as follows:

   A 1.27cm wall thickness cylindrical barrel with the outer-diameter of 91.44cm and the overall height of 71.07cm is filled with sand up to its top. A 100g cylindrical-disk shape C4 high-energy explosive is buried into the sand along the centerline of the barrel with its faces parallel with the sand surface. The depth of burial (defined as a distance between the top face of the explosive and the sand surface) is varied in a range between 0 and 8cm. A set of five pressure transducers is utilized to monitor the pressure in the air above the sand and within the sand following detonation of the explosive. Three of these transducers are located in the air and two in the sand. The position coordinates of the three transducers used in air and the two transducers used in sand are given in Table 1. The transducers located in the air are denoted as PA1 through PA3 while those located in the sand are denoted as PS1 through PS2. It should be noted that, in order to be consistent with the definition of coordinate system used in AUTODYN [2], the y coordinates are measured in the radial direction from the centerline of the barrel, while the x coordinates are measured along the centerline, with x=0 corresponding to the sand surface and x>0 denoting the air region above the sand.
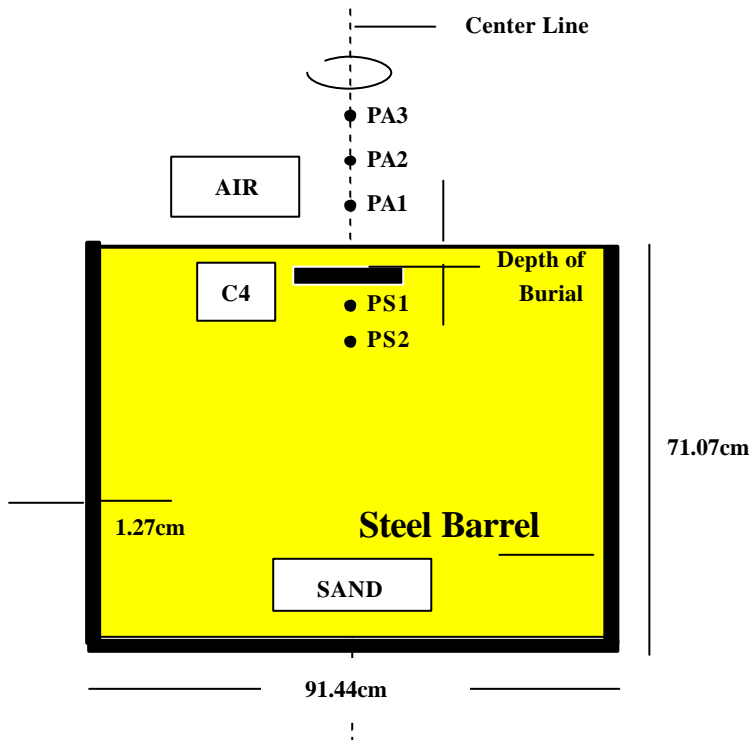
Fig.1. A simple schematic of the experimental setup used in Ref. [1] to study the effect of explosion of a shallow-buried mine. Please note that the locations of the pressure transducers PA1, PA2, PA3, PS1 and PS2 are not drawn to scale.

Table1. Coordinates of the Pressure Transducers located in air (PA1-PA3) and in the soil (PS1-PS2). The Origin of the Coordinate system is located along the line of symmetry at the Soil/Air interface.

Transducer Designation	Transducer Coordinates, cm	
	x	y
PA1	30.00	0
PA2	110.00	0
PA3	190.00	0
PS1	$-8.93 - x_b^*$	0
PS2	$-13.93 - x_b^*$	0

$*x_b$ is the Depth of Burial (DOB) i.e., distance from the top of the explosive to the soil/air interface

The computational domain used to represent the physical model shown in Fig.1 is displayed in Fig.2. Due to the inherent cylindrical symmetry of the problem, a two dimensional axisymmetric model is developed. The right boundary in Fig.2 coincides with the axis of symmetry (x-axis). The horizontal direction (y-axis) corresponds to the radial direction.

The computational domain displayed in Fig.2 is analyzed using an Euler grid, which enables the existence of several materials (a multi-material option) within the same grid cell. The availability of this option may be critical when explosion is modeled since, following detonation, the gaseous detonation products, soil and air may simultaneously reside in the same grid cells in many portions of the computational domain.

Due to a large wall thickness of the steel barrel which confines the soil within the barrel in the radial direction, the "no flow" boundary conditions are applied along the portions of the computational domain boundaries which coincide with the barrel. For the remaining portions of the computational-domain boundaries, the "flow out" boundary conditions are applied.

Different portions of the computational domains are filled with the three materials (C4, sand and air) in accordance with the physical problem defined in Fig.1. The constitutive equations pertaining to the response of the three materials to a (hydrostatic) pressure, a deviatoric stress and/or a negative pressure are discussed in some details in Section 2.3.

To mimic the detonation initiation conditions used in Ref. [1], detonation is initiated at the central circular portion of the explosive of radius 3.1cm, at the bottom of the explosive.

2.3. *Materials Constitutive Models*

Hydrodynamic computer programs such as AUTODYN [2] are capable of predicting an unsteady, dynamic motion of a material system by solving the appropriate mass, momentum and energy conservation equations, subjected to the associated initial and boundary conditions. However, for the aforementioned boundary value problem to be fully defined, additional relations between the flow variables (pressure, density, energy, temperature, etc.) have to be defined. These additional relations typically involve an equation of state, a strength equation and a failure equation for each constituent material. These equations arise from the fact that, in general, the total stress tensor can be

decomposed into a sum of a hydrostatic stress (pressure) tensor (which causes a change in the volume/density of the material) and a deviatoric stress tensor (which is responsible for the shape change of the material). An equation of state then is used to define the corresponding functional relationship between pressure, density and internal energy (temperature), while a strength relation is used to define the appropriate equivalent plastic-strain, equivalent plastic-strain rate, and temperature dependences of the equivalent deviatoric stress (or some function of it). In addition, a material model generally includes a failure criterion, i.e. an equation describing the (hydrostatic or deviatoric) stress and/or strain condition which, when attained, causes the material to fracture and loose its ability to support normal and shear stresses.
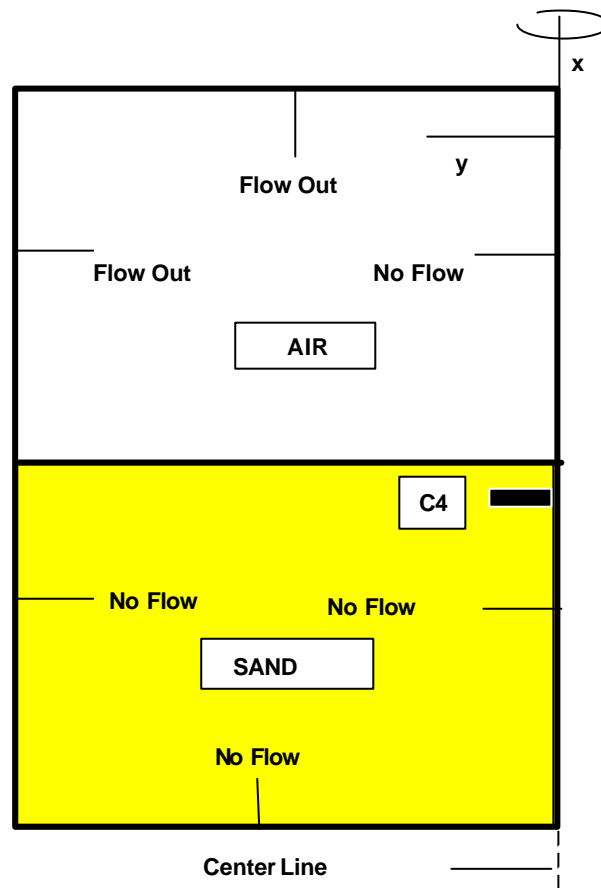
Fig.2. A simple schematic of the two-dimensional axisymmetric computational domain along with the boundary conditions used in the numerical modeling of the physical problem depicted in Fig.1.

In the present work the following materials are utilized within the computational domain: air, sand and C4 (a high-energy explosive material). In the remainder of this section, a brief description is given of the models used for each of the three constituent materials.

Air is modeled as an ideal gas and, consequently, its equation of state is defined by the ideal-gas gamma-law relation as [6]:

$$P = (g - 1)\frac{r}{r_0}E \qquad (1)$$

where P is the pressure, g the constant-pressure to constant-volume specific heats ratio (=1.4 for a diatomic gas like air), r_0 (=1.225kg/m^3) is the initial air density, and r is the current density. For Eq. (1) to yield the standard atmosphere pressure of 101.3kPa, the initial internal energy E is set to 253.4kJ/m^3 which corresponds to the air mass specific heat of 717.6J/kg·K and a reference temperature of 288.2K.

Since air is a gaseous material and has no ability to support either shear stresses or negative pressures, no strength or failure relations are required for this material.

The Jones-Wilkins-Lee (JWL) equation of state is used for C4 in the present work since that is the preferred choice for the equation of state for high-energy explosives in most hydrodynamic calculations involving detonation. The JWL equation of state is defined as [7, 8]:

$$P = A\left(1 - \frac{w}{R_1 v}\right)e^{-R_1 v} + B\left(1 - \frac{w}{R_2 v}\right)e^{-R_2 v} + \frac{wE}{v} \qquad (2)$$

where the constants A, R_1, B, R_2 and w for C4 are defined in the AUTODYN material library and v is the specific volume of the material.

As explained earlier, within a typical hydrodynamic analysis, detonation is modeled as an instantaneous process which converts unreacted explosive into gaseous detonation products and detonation of the entire high-explosive material is typically completed at the very beginning of a given simulation. Consequently, no strength and failure models are required of high-energy explosives such as C4.

Sand is a porous granular material. The equation of state for sand used in the present work is based on a piece-wise linear pressure-density relation. It should be noted that this relation is equivalent to the standard Mie-Gruneisen equation of state in which the Gruneisen gamma parameter, $\Gamma = v\left(\frac{\partial P}{\partial E}\right)_v$ is set to zero [2]. Thus, the present model ignores an increase in the pressure of a porous material like sand due to absorption of the energy. This means that the present model would give a more reliable material response under the conditions when either the energy absorbed is not very high (e.g. when the applied pressure levels are not significantly larger than the pressure levels at which the porous material crushes and compacts into a solid material), when the initial material porosity is small or when the magnitude of the Gruneisen gamma parameter is near zero. The piece-wise linear equation of state is implemented within AUTODYN using up to ten (r, P) pairs of values.

The strength model for sand is based on an isotropic, perfectly plastic, rate independent yield-surface approximation. Following Laine et al. [10], the yield stress is assumed to depend explicitly only on pressure and not on density of the porous material. Within the AUTODYN program [2], the relationship between the yield stress, Y, and

pressure, P, is defined as a piece-wise linear function consisting of up to ten (P, Y) pairs of values. The yield stress is proportional to the second invariant of the deviatoric part of the stress tensor and quantifies the resistance of the material to a plastic (irreversible) shape change.

Unloading (and subsequent reloading) of a previously plastically deformed material is of an elastic (reversible) nature and, in this case, the deviatoric stress is proportional to the deviatoric strain with the proportionality constant being equal to the shear modulus, G. In a porous material such as sand, the shear modulus is a function of the material density. Hence, the strength model for sand entails specification of not only the Y vs. P relation but also the G vs. r relation. The G vs. r relation is defined within AUTODYN [2] as a piece-wise linear function using up to ten (r, G) pairs of data.

The failure behavior of sand is modeled within the AUTODYN materials database by specifying a minimum (negative) value of the hydrodynamic pressure below which, the material fractures, and looses its ability to support any tensile or shear stress. However, if a given "fractured" material region is subsequently subjected to positive pressures, it is given an ability to reheal and close up its cracks. In addition to the minimum (negative) pressure failure model few other failure models for sand are examined in the present work.

2.4. Computational Method

All the calculations carried out in the present work are done using AUTODYN, a state of the art non-linear dynamics modeling and simulation software [2]. AUTODYN is a fully integrated engineering analysis computer code which is particularly suited for modeling the explosion, blast, impact and penetration events. Codes such as AUTODYN are commonly referred to as "*hydrocodes*". Within the code, the appropriate mass, momentum and energy conservation equations coupled with the materials modeling equations and subjected to the appropriate initial and boundary conditions are solved. The numerical methods used for the solution of these equations involve finite difference, finite volume and finite element methods and the choice of the method used (i.e. "*processor*" as referred to in AUTODYN) depends on the physical nature of the problem being studied. The power of AUTODYN is derived mainly from its ability to handle complex problems in which different regions can be analyzed using different methods.

3. RESULTS AND DISCUSSION

3.1. Early Soil-Deformation Stage

The present computational results pertaining to the early deformation stage of the soil are presented and discussed in this section. In addition, the corresponding experimental results obtained using x-ray photography in Ref. [1] are presented for comparison. In all the cases analyzed a fixed 100g weight of C4 high-energy explosive was used. To enable a comparison between the computational and experimental results, two depths of burial (3cm and 8cm) were used.

Profiles of the soil bubble at different times following the detonation of C4 explosive for the depth of burial values of 3cm and 8cm are shown respectively in Figs 3(a)-(b) and Figs 4(a)-(b). For both Figs 3 and 4, the part (a) contains the experimental results from Ref. [1], while the part (b) contains the present AUTODYN-based computational analysis results.
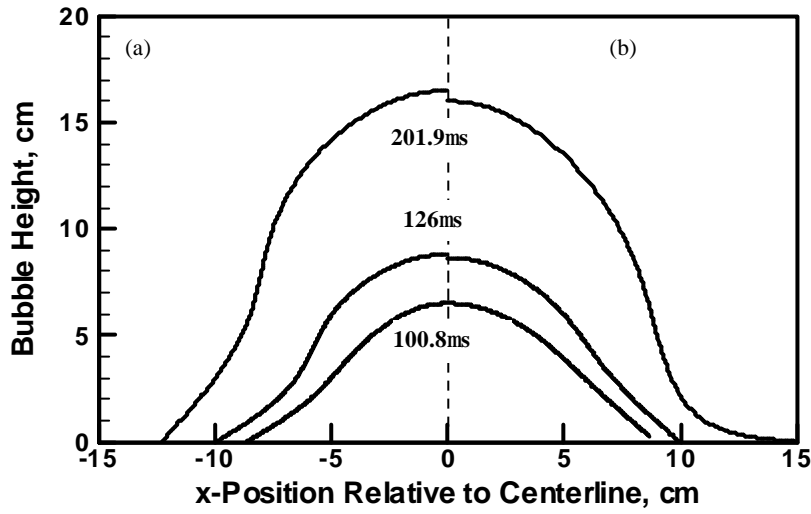
Fig.3. A comparison of the soil-bubble profiles at different times following detonation of 100g of C4 high-energy explosive at depth of burial of 3cm: (a) Experimental results from Ref. [1] and (b) the present AUTODYN-based computational results.
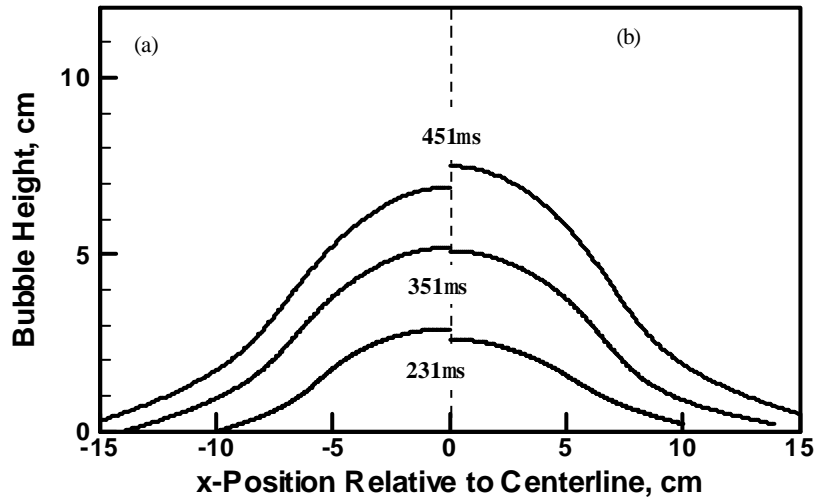
Fig.4. A comparison of the soil-bubble profiles at different times following detonation of 100g of C4 high-energy explosive at depth of burial of 8cm: (a) Experimental results from Ref. [1] and (b) the present AUTODYN-based computational results.

A brief examination of the results displayed in Figs 3 and 4 shows that, in general, there is a reasonably good agreement between the experimental results and their computational counterparts. This is particularly the case considering the fact that the experimental results are associated with a considerable ($\pm$ 10 %) variation. In addition, the experimental data reported in Ref. [1] contain only the information pertaining to the bubble width at four distinct vertical locations. This made a precise definition of the bubble shape somewhat uncertain. Nevertheless, it appears that the experimental and the computational results are in a reasonably good agreement relative to the overall shape and size of the soil bubble.

A comparison between the (maximum) bubble heights obtained experimentally and computationally for the two values of depth of burial is depicted in Fig.5. The experimental results are displayed using individual symbols, while the computational results are denoted using solid lines. Based on the results displayed in Fig. 5, it can be established that the present AUTODYN-based calculations quite accurately account for the early deformation stage of the soil.

A reasonably good agreement is also found between the experimental and computational results with respect to the time of onset of formation of the soil bubble. Namely, for the 3cm and 8cm depths of burial, such times were found to be 25μs and 79μs respectively using the AUTODYN calculations, while the corresponding experimental times reported in Ref. [1] are 30μs and 79μs.
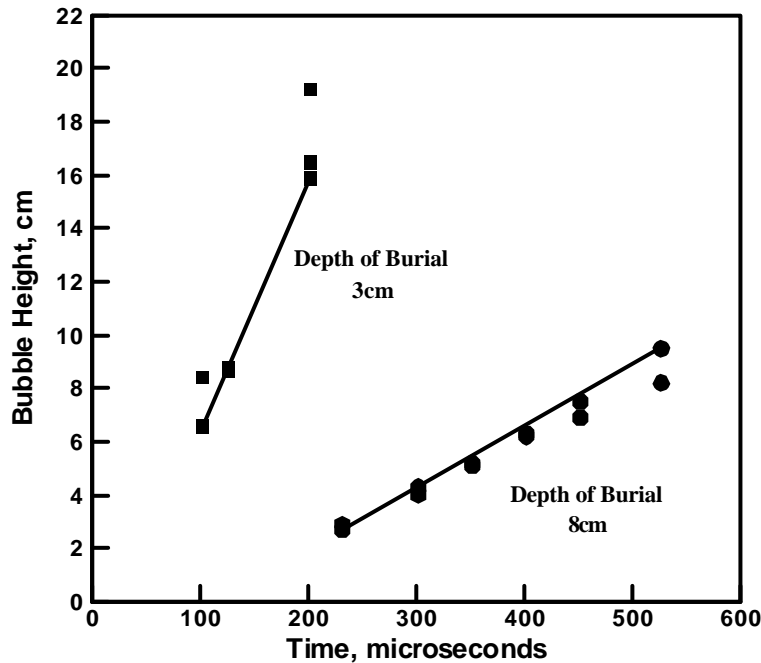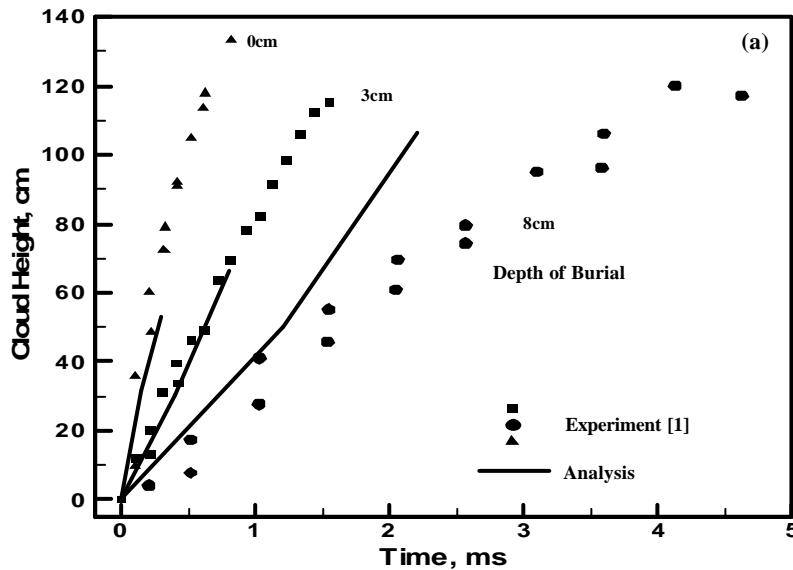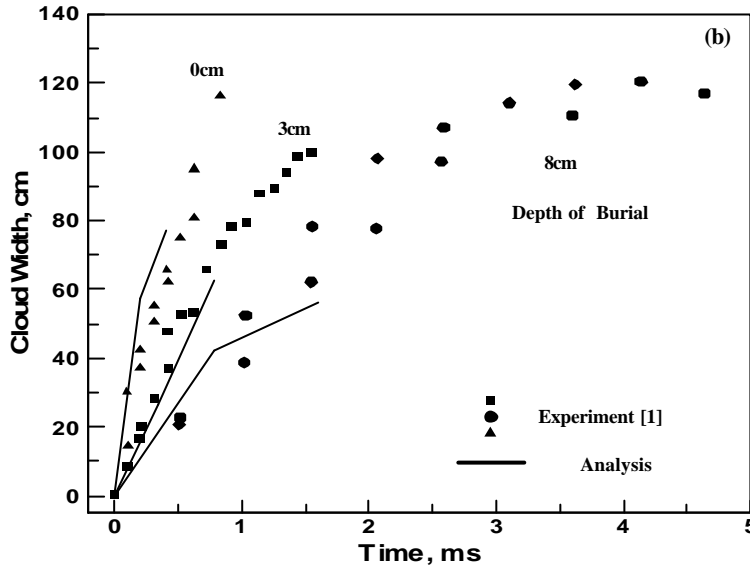

Fig.5. Variation of the soil-bubble height with time following detonation of 100g of C4 high-energy explosive for two different depths of burial. Scattered points represent experimental data from Ref. [1], while the solid lines denote the present AUTODYN based computational results.

3.2. Expansion of the Detonation Products

As the height of the soil bubble increases, the thickness and, thus, the strength of the soil layer above the gaseous detonation products decreases. This ultimately leads to the fracture of the soil bubble and to the venting and expansion of the detonation products into the air above the soil (i.e. to the formation of a gas cloud). The present computational results pertaining to this stage of the detonation process are presented and discussed in this section. For comparison the corresponding experimental results obtained using high-speed photography reported in Ref. [1] are also presented. The process parameters used include a 100g C4 charge weight and three depths of burial (0cm, 3cm and 8cm). A comparison of the computational and the experimental results pertaining to the height and to the width of the detonation-gas cloud for the three values of depth of burial are shown respectively in Figs 6(a)-6(b). The experimental results displayed in Figs 6(a)-(b) are shown as individual symbols while the computational results are denoted using solid lines. It should be noted that the maximum simulation times were limited by the size of the computational domain and by the requirement that the detonation gas cloud is fully contained within the computational domain. The results displayed in Fig. 6(a) show that there is a reasonably good agreement between the experimental and computational results for the depths of burial of 0cm and 3cm for the variation of cloud height (although the computed cloud heights are somewhat lower than their experimental counterparts). On the other hand, the computed cloud heights at longer simulation times are significantly higher than their experimental counterparts in the case of 8cm depth of burial.

The results displayed in Fig.6 (b) show that the best agreement between the computed and the experimental cloud widths is obtained in the case of 3cm depth of burial. In the flush charge case (0cm depth of burial) the computed cloud widths are somewhat higher than their experimental counterparts. The opposite appears the case for 8cm depth of burial.

Fig.6. A variation of: **(a)** the cloud height and **(b)** the cloud width with time following detonation of 100g of C4 high-energy explosive for three values of depth of burial. Experimental data from Ref. [1] are denoted using individual symbols while the present computational results are shown as solid lines.

3.3. Soil Ejection Stage

The last stage of detonation of the shallow buried explosive involves substantial ejection of the soil in the upward direction. The present computational results pertaining to this stage of the detonation process are presented and discussed in this section. For comparison the corresponding experimental results reported in Ref. [1] are also presented. The process parameters such as the charge weight and depth of burial are identical to those reported in Section 3.2. It should be noted that due to the size limitation of the computational domain and the requirement that the soil-fragment laden detonation-gas cloud fully resides within the computational domain no computational results pertaining to the size of the cloud are reported. Rather the results pertaining to the magnitude of the included angle of the cloud are reported and compared with their experimental counterparts.

Temporal evolution of the gas-cloud included angle for the three values of the depth of burial are displayed in Fig.7. The results displayed in Fig.7 can be summarized as follows:

(a) As the depth of burial increases, the motion of the detonation products within the gas-cloud becomes more directed in the upward direction leading to smaller values of the included angle. This behavior is observed in both the experimental and computational results;

(b) At the early stages of cloud formation, the experimental results show that included angle does not change significant with time, while, at the longer times, the included angle decreases with time. With the exception of the case of 0cm depth of burial, the computed results are generally in good agreement with their experimental

counterparts regarding the temporal variation of the included angle. As explained earlier, due to the limitations associated with the size of the computational domain, long time data for the included angle were not computed in the present work; and

(c) In general, the computed included angles are significantly lower than their experimental counterparts, although, the agreement between the computed and experimental results appears more reasonable for the case of 8cm depth of burial. It should be noted that the typical shape of the gas-cloud deviates significantly from an inverted cone shape which contributes significantly to the uncertainty in the computed and the experimentally measured included angles.
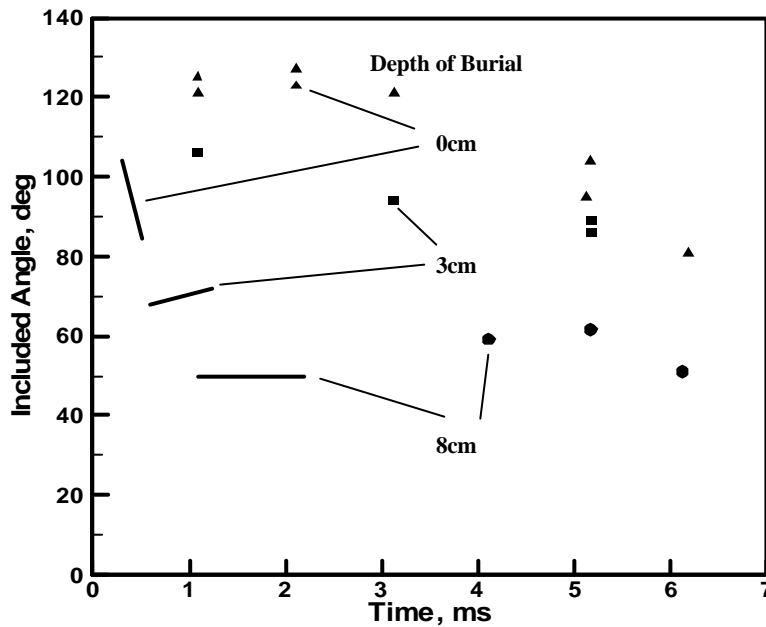
Fig.7. Temporal variation of the gas-cloud included angle for the three values of depth of burial. Experimental data from Ref. [1] are denoted using individual symbols while the present AUTODYN-based computational results are shown as solid heavy lines.

3.4. Shock Pressure and Impulse in Air

Temporal variations of the shock pressure and impulse in air at the locations of the three pressure transducers (PA1, PA2 and PA3) are presented and discussed in this section. The spatial coordinates of the three transducers are given in the Table 1. It should be recalled that the origin of the coordinate system is located along the axis of symmetry at the initial sand/air interface. For comparison, the variations of the corresponding hydrostatic (side on) pressures with time experimentally determined in Ref. [1] are also presented in this section.

The temporal variations of the pressure at the locations of the three pressure transducers in air in the case of a 0cm depth of burial are shown respectively in Figs 8(a)-(c). In Figs 8(a)-(c), the experimental results obtained in Ref. [1] are denoted by dashed lines while the present AUTODYN-based computational results are shown as

solid lines. It should also be noted that the results displayed in Figs 8(a)-(c) pertain to the overpressure, i.e. the difference between the local hydrostatic pressure and 1atm hydrostatic pressure. The same type of overpressure vs. time traces was generated for the other two depths of burial (3cm and 8cm). These results are not included for brevity. Rather, a summary plot showing the variation of the peak overpressure at the location of three pressure transducers for the three values of the depth of burial are displayed in Fig. 9. In each case a set of three experimental results corresponding to the nominally identical conditions of charge weight, depth of burial and the pressure transducer location are displayed in Fig.9. The results displayed in Figs 8(a)-(c) and 9 (as well as in the overpressure vs. time traces not shown for brevity) can be summarized as follows:

(a)   There is a significant scatter in the experimental results obtained in Ref. [1] under nominally identical conditions;

(b)   Despite the aforementioned scatter in the experimental results, the computed peak pressures are typically lower than their experimental counterparts;

(c)   Computed times of arrival of the shockwave at the locations of the pressure transducers PA1, PA2 and PA3 are typically longer than their experimental counterparts;

(d)   The computed positive phase durations (the time periods over which the overpressure is positive) are generally comparable with their experimental counterparts;

(e)   At the locations of the pressure transducers PA1 and PA2 which are closest to the sand/air interface, the computed overpressure traces consist of a single peak followed by a gradual decrease in overpressure, Figs 8(a)-(b). This overpressure decrease continues into the negative range of overpressure and ultimately the overpressure begins to increase and ultimately approaches a zero value in an asymptotic fashion. It should be noted that the long-time portions of the overpressure traces are not displayed in Figs 8(a)-(b) for improved clarity;

(f)   In the case of the pressure transducer PA3 which is the farthest from the sand/air interface the overpressure trace consists of two peaks of comparable heights, Fig. 8(c). After the second peak, the overpressure continues to decrease and the overpressure vs. time behavior is similar to those in Figs 8(a)-(b); and

(g)   A close examination of the results displayed in Figs 8(a)-(b) suggests that the apparent single overpressure peak is likely a superposition of two closely spaced peaks. The existence of two closely spaced (unresolved or resolved) overpressure peaks is found to be the result of two shock waves originating at the detonation products/air interface. The first shock wave was caused by the initial detonation wave which converts the solid C4 high-energy explosive into high-pressure detonation products. A careful examination of the pressure fields during the simulation of the explosion process revealed that the second shock wave in air was caused by a second compression wave in the detonation products colliding with the detonation-products/air interface. The formation of the second compression wave appears to follow the following sequence of events: (i) A rarefaction wave is initially generated at the detonation-products/air interface as a result of acoustic impedance mismatch between the detonation products and air; (ii) The rarefaction wave travels through the detonation products in the downward direction until it collides with the detonation-products/sand interface; and (iii) A compression wave is then generated in the detonation products at the detonation-products/sand

interface which travels in the upward direction until it impinges on to the detonation-products/air interface creating the second shock wave in air.

In addition to computing the overpressure vs. time traces, the impulses vs. time traces at the location of three pressure transducers were also determined. These were obtained by integrating the corresponding overpressure vs. time results. The individual resulting plots will not be shown here for brevity; instead, a summary plot displaying the effect of the depth of burial and distance from the sand/air interface on the peak value of the impulse is given in Fig.10.
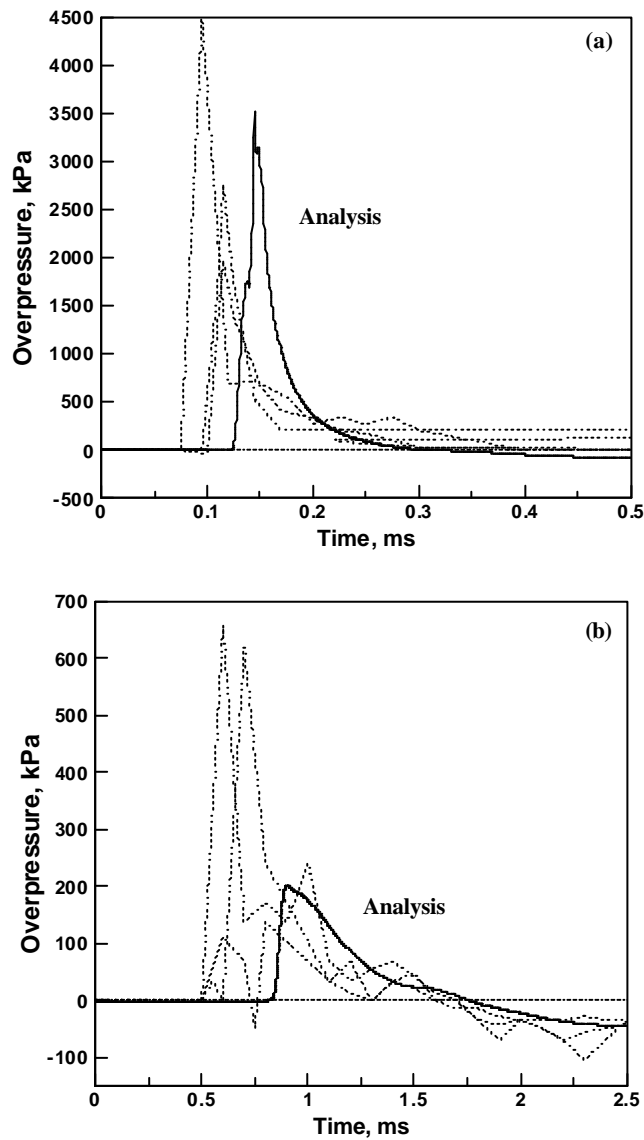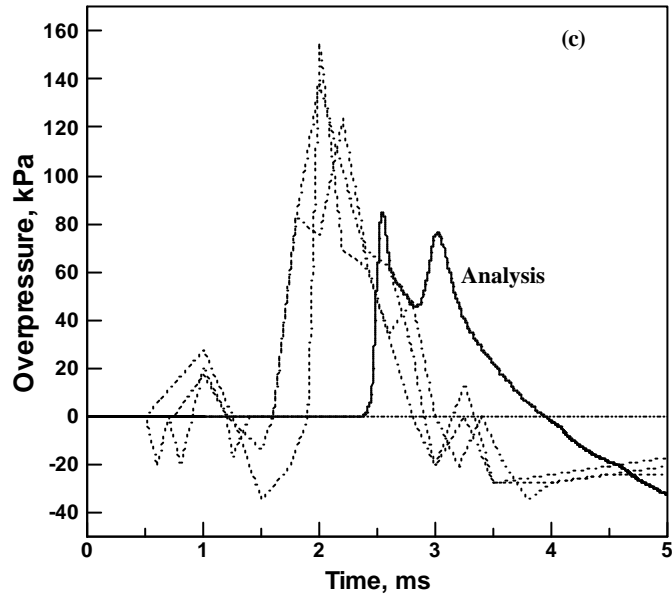
Fig.8. Variation of the side-on pressures in air with time following detonation of 100g of C4 high-energy explosive at the depth of burial of 0cm at the location of the pressure transducers: **(a)** PA1 **(b)** PA2 and **(c)** PA3. Please consult Table. 1 for the coordinates of the pressure transducers.
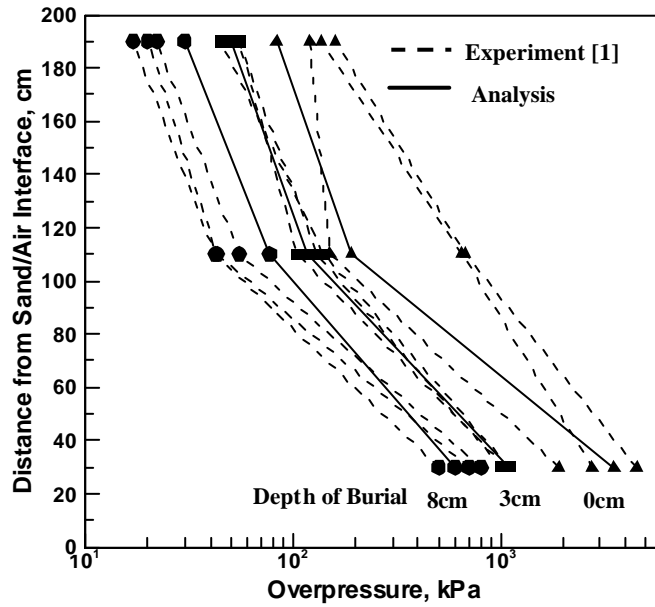
Fig.9. Variation of the side-on pressures in air with distance from sand/air interface and depth of burial.
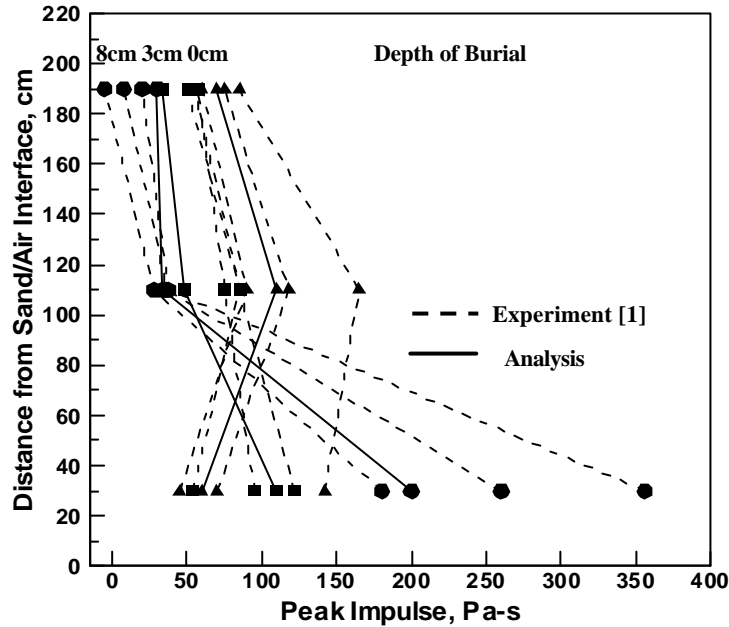
Fig.10. Variation of the peak impulse in air with distance from sand/air interface and depth of burial.

The result displayed in Fig.10 show that, while there is a substantial scatter in the experimental results, the agreement between the computed peak impulse values and their experimental counterparts is relatively good. In addition, there is an interesting trend regarding the effect of the depth of burial at the peak impulse value at different distances from the sand/air interface. At the shortest distances from the sand/air interface, the largest peak value of the impulse corresponds to the largest charge depth of burial. Conversely, at the largest distances from the sand/air interface, the largest peak value of the impulse corresponds to the 0cm depth of burial. This finding appears to be related to the effect of the sand bubble and the vents within it in directing the detonation-products gases in the upward direction. This effect is strongest at the shortest distances from the sand/air interface and despite the shortest arrival times and some energy losses due to gas/sand interactions, the resulting peak impulse values are the largest. At the longest distances from the sand/air interface, the effect of sand bubbles is diminished relative to the effects of energy loss due to gas/sand interaction, and consequently the largest peak values of the impulse are obtained for the case of 0cm depth of burial.

3.5. Shock Pressure and Impulse in Sand

Temporal variations of the shock pressure and impulse in sand at the locations of the two pressure transducers (PS1 and PS2) are presented and discussed in this section. The spatial coordinates of the two transducers are given in the Table 1. It should be recalled that the origin of the coordinate system is located along the axis of symmetry at the initial sand/air interface. For comparison, the variations of the corresponding hydrostatic

(side on) pressures with time experimentally determined in Ref. [1] are also presented in this section.

The temporal variation of the pressure at the locations of the two pressure transducers in sand in the case of a 0cm depth of burial are shown respectively in Figs 11(a)-(b). In Figs 11(a)-(b), the experimental results obtained in Ref. [1] are denoted by dashed lines while the present AUTODYN-based computational results are shown as solid lines. It should also be noted that the results displayed in Figs 14(a)-(b) pertain to the overpressure, i.e., the difference between the local hydrostatic pressure and 1atm hydrostatic pressure. The same type of overpressure vs. time traces was generated for the other two depths of burial (3cm and 8cm). These results are not included for brevity. Rather, a summary plot showing the variations of the peak overpressure at the location of two pressure transducers for the three values of the depth of burial are displayed in Fig.12. In each case, a set of three experimental results corresponding to the nominally identical conditions of charge weight, depth of burial and the pressure transducer locations are displayed in Fig.12. The results displayed in Figs 11(a)-(c) and 12 (as well as in the overpressure vs. time plots not shown for brevity) are discussed in the remainder of this section.

Before a discussion is presented regarding the level of agreement between the experimental and the computed overpressure traces in the sand, it should be noted that the pressure transducer PS1 was located very near the charge in the experimental investigation reported in Ref. [1]. Consequently, it was typically observed that the pressure transducer at the location PS1 suffers a significant mechanical damage; in addition, a layer of carbon residue was found coating the surfaces of the pressure transducer. These findings suggest the pressure transducer PS1 was most likely located in the hydrodynamic zone of deformation in the sand and subjected to significant thermal loads. Consequently, the experimental results obtained using these pressure transducers are not expected to be as reliable as those obtained using the pressure transducer PS2. The latter transducer was typically found not to suffer any observable mechanical damage or be subjected to a significant thermal load.

In general, the overall agreement between the computed and the experimental overpressure vs. time traces is reasonable considering the fact that there is a substantial scatter in the experimental results. Typically, the computed maximum overpressure values, the times of arrival and the positive phase durations are bracketed by their corresponding experimental counterparts. There are at least two characteristics of the overpressure traces in which the computed and experimental results differ:

(i) The computed overpressure traces typically show multiple minor peaks following the initial main pressure peak. While such multiple minor peaks are typically not seen in the experimental data, a close examination of the experimental overpressure traces suggests that such peaks may exist but, due to their large width and relatively small spacing, are not resolved. In any case, the formation of the multiple peaks is the result of a complex interactions of compression waves and rarefaction waves within the sand; and

(ii) The computed overpressure traces at the location of pressure transducer PS1 often contain portions consisting of a sharp over pressure drop to a zero value followed by a zero level of overpressure, Figs 11(a). No such behavior is observed in the experimental overpressure traces. A careful examination of the pressure fields during simulation of the detonation process revealed that the behavior is a result of the superposition of a

compression wave and a rarefaction wave approaching each other. As mentioned earlier the pressure transducer PS1 was subjected to major mechanical and thermal loads and, hence, the experimental information obtained from this transducer in less reliable. It is, hence, possible that the transducer PS1 was unable to detect fine details on the temporal variation of overpressure.
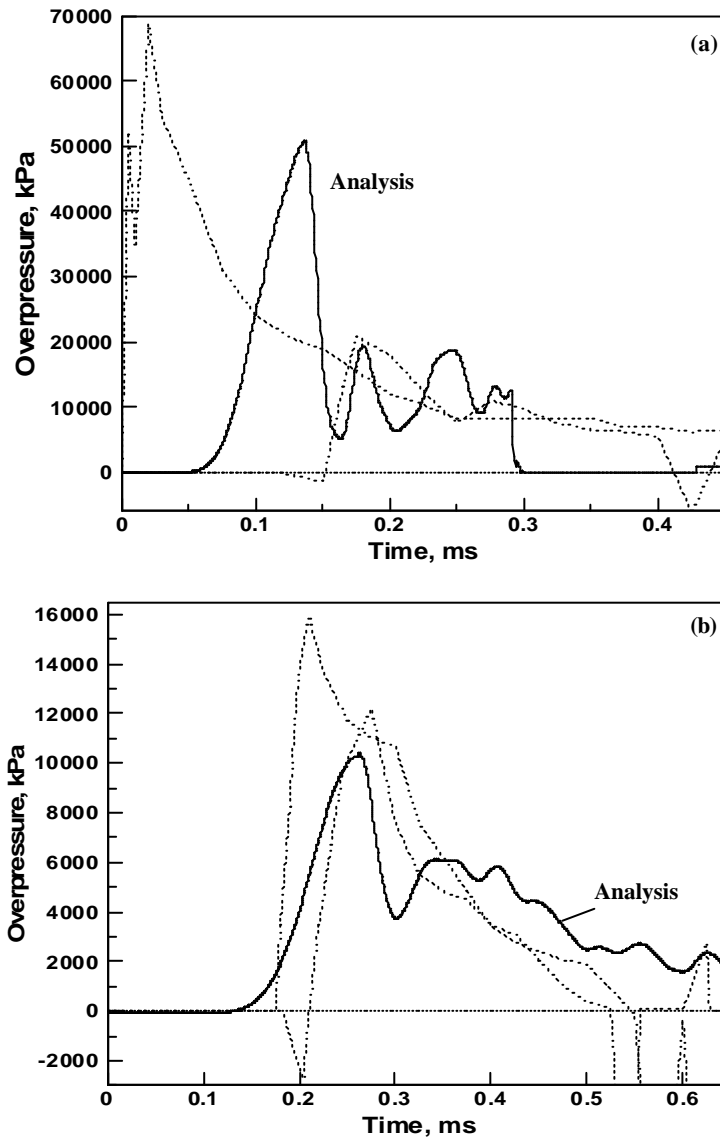
Fig.11. Variation of the side-on pressures in the sand with time following detonation of 100g of C4 high-energy explosive at the depth of burial of 0cm at the location of the pressure transducers: **(a)** PS1 and **(b)** PS2. Please consult Table. 1 for the coordinates of the pressure transducers.
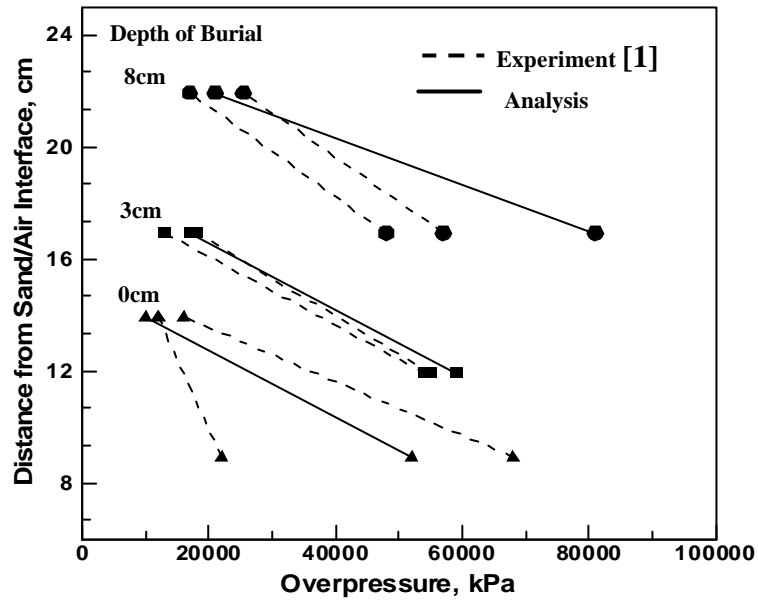
Fig.12. Variation of the side-on pressures in soil with distance
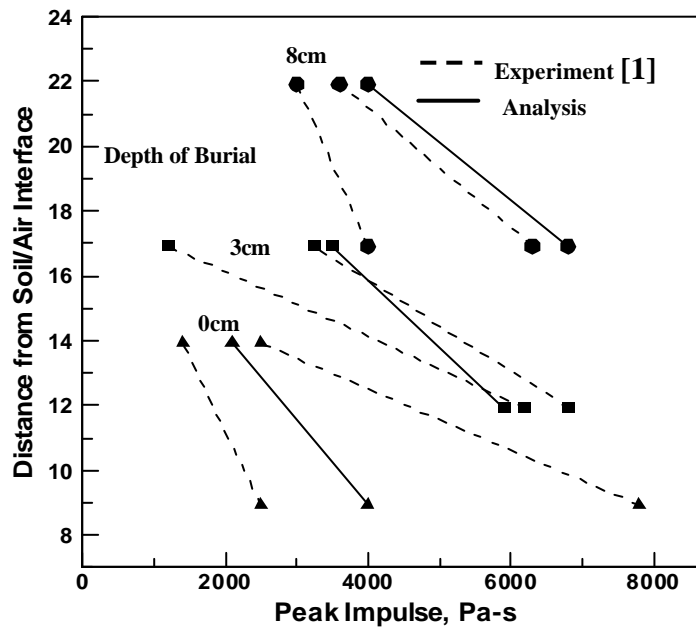from sand/air interface and depth of burial.

Fig.13. Variation of the peak impulse in soil with distance
from sand/air interface and depth of burial.

In addition to computing the overpressure vs. time traces, the impulses vs. time traces at the location of two pressure transducers were also determined. These were obtained by integrating the corresponding overpressure vs. time results. The individual resulting plots will not be shown here for brevity. Instead, a summary plot displaying the effect of the depth of burial and distance from the sand/air interface on the peak value of the (pressure) impulse is given in Fig.13. In general, the same type of comments can be made regarding the level of agreement between the experimental and computed impulse vs. time results as those made in the case of overpressure vs. time results.

3.6. Size of the Crater

As discussed earlier, a significant portion of the momentum transfer to the target structure/personnel is carried out by the ejected sand. It is hence important to quantify the volume of the sand which is displaced as a result of the explosion of a shallow-buried mine. In this section, the results pertaining to the size of the crater generated within the sand are presented and discussed. For comparison, the corresponding experimental results obtained in Ref. [1] are also presented.

The morphology of the craters resulting from detonation of 100g of C4 high-energy explosive at 0cm, 3cm and 8cm depths of burial experimentally determined in Ref. [1] are displayed in Figs 14(a)-(c), respectively. The results displayed in Figs 14(a)-(c) can be summarized as follows:

(a) For each of the three values of depth of burial, the crater width extends up to the diameter of the barrel;

(b) The depth of the crater increases slightly with an increase in the depth of burial from approximately 16 cm, in the case of 0cm depth of burial, to approximately 17cm, in the case of 8cm depth of burial; and

(c) For the cases of 0cm and 3cm depth of burial, the central portion of the crater appears to be nearly flat, Figs 14(a)-(b), while for the case of 8cm depth of burial, Fig. 14(c), the central portion of the crater contains a minor bulge.

The corresponding AUTODYN-based computational results are displayed in Figs 15(a)-(c). To help interpretation of the results displayed in Figs 15(a)-(c), a thin horizontal line is used to indicate the initial sand/air interface. The results displayed in Figs 15(a)-(c) differ from their experimental counterparts displayed in Figs 14(a)-(c) in several respects:

(a) The computed sand craters (defined with respect to the initial position of the sand/air interface) do not extend out to the barrel walls;

(b) The computational results show that some displaced sand remains above the initial position of the sand/air interface;

(c) While the computational results show an increase in the crater depth with an increase in depth of burial, in agreement with the experimental results, this variation is substantially more pronounced in the case of the computational results.

(d) The computed values of the crater depth at low values of depth of burial, Figs 15(a)-(b), are substantially lower than their experimental counterparts, Figs 14(a)-(b); and

(e) While the computed crater shape for the largest depth of burial, Fig.15(c), shows a bulge at its bottom in agreement with the corresponding experimentally determined crater shape shown in Fig.14(c), the height of the computed bulge is clearly larger.

The observed discrepancies between the computational and experimental shapes of the sand craters should be at least partly due to the inability of the materials model for sand defined in the AUTODYN [2] materials library to realistically represent the dynamic mechanical response of 3050 mesh high purity silica sand with an average moisture content of 0.4%, which was characterized as being able to flow "like-a-fluid" in Ref. [1]. Moisture typically increases the cohesive strength of sand but can lower the sand's shear strength by acting as an inter-particle lubricant. To illustrate the potential effect moisture can have on the shapes of sand craters, the original yield stress vs. pressure data defined in AUTODYN materials library are modified by dividing the yield stress values by a factor of two. The computed crater shapes for the three values of depth of burial and the modified sand constitutive model are shown in Figs 16(a)-(c). While it may appear that the division of the yield stress of the sand by a factor of two is quite arbitrary, it should be noted that sand properties such as the average particle size, particle size distribution and the moisture content can readily give rise to multifold changes in the sand strength [9, 10].
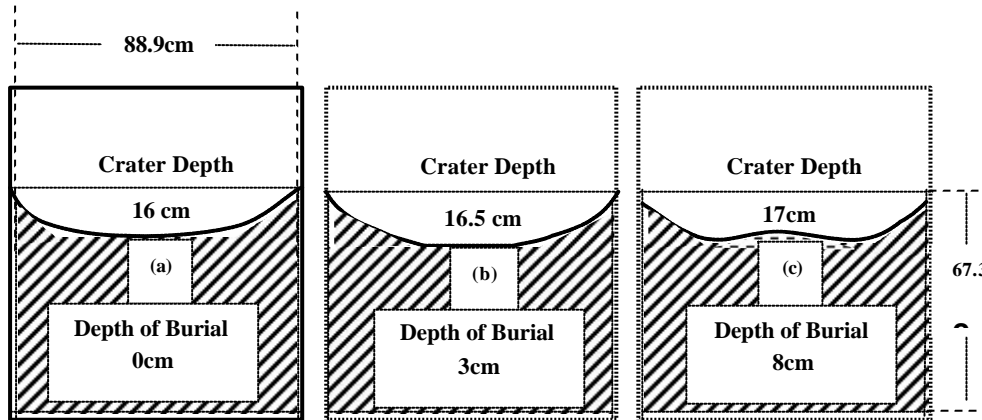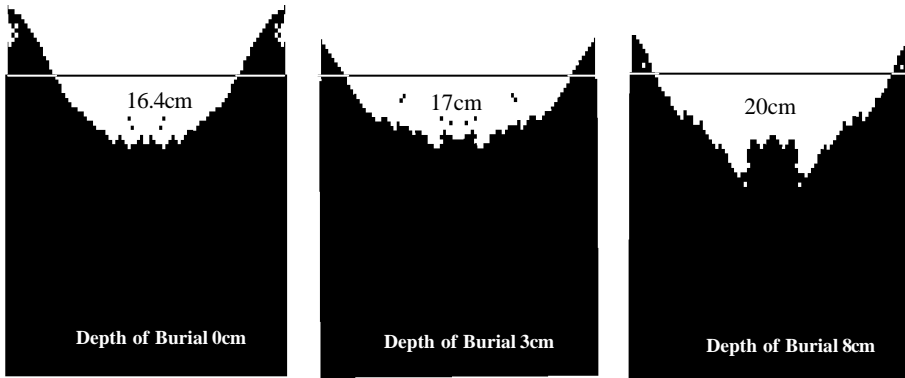

Fig.14. The shape of the sand craters for the three values of depth of burial:
(**a**) 0cm; (**b**) 3cm; (**c**) 8cm obtained experimentally in Ref. [1].
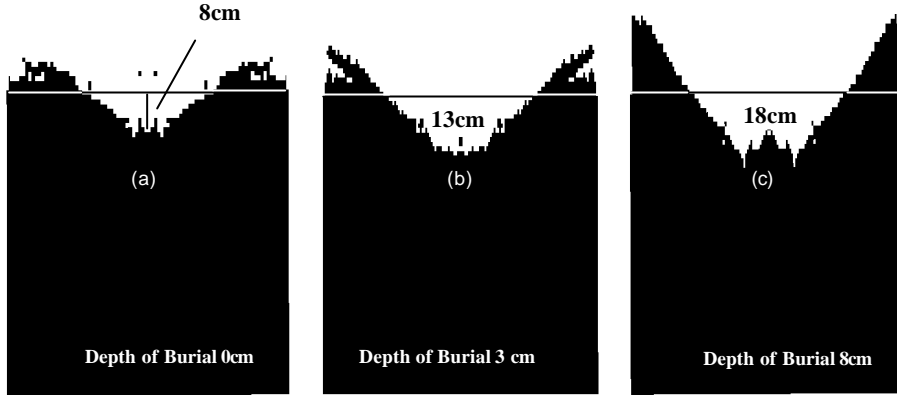
Fig.15. The shape of the sand craters for the three values of depth of burial: **(a)** 0cm; **(b)** 3cm; **(c)** 8cm obtained in the present work using AUTODYN-based calculations and the original sand materials constitutive relations as defined in the AUTODYN materials database.


Fig.16. The shape of the sand craters for the three values of depth of burial: **(a)** 0cm; **(b)** 3cm; **(c)** 8cm obtained in the present work using AUTODYN-based calculations and the modified materials constitutive relations for sand. Please see text for details.

It should be noted that the experimental results shown in Figs 14(a)-(c) correspond to the final crater shapes while the computed crater shapes displayed in Figs 15(a)-(c) and 16(a)-(c), are obtained after simulation times of 150ms. To obtain a more quantitative comparison between the measured and computed crater shapes, the corresponding variations in the crater depth and the crater width with the charge depth of burial are displayed in Figs 17 and 18, respectively. It should be noted that the experimental crater depths correspond to their final values while the experimental crater widths correspond to the time of 12ms following denotation, the time which was matched in the computational analysis. Hence, obtaining a better agreement with respect to the crater width between the experiment and the analysis is more critical. By analyzing the results displayed in Figs 14-18, the following main observations can be made:

(a) In general, the agreement between the predicted sand crater shapes based on the modified sand material model and their experimental counterparts is improved relative to the corresponding agreement based on the original sand constitutive relations;

(b) The improvement is particularly pronounced at smaller values of the charge depth of burial; and

(c) The computed sand crater shape and size appear to be fairly sensitive functions of the sand materials constitutive model used. The findings made above suggest that a good agreement between the computed and experimental sand crater shapes and sizes should be expected only when reliable materials constitutive models for the sand in question are used in the calculations. Such constitutive models should include the effects of the sand particle size, shape and their orientation, impurity and moisture contents, etc. Once such materials constitutive relations are available, one can carry out a sensitivity analysis to determine how the potential variations in the sand structure and properties affect its behavior during an explosion.
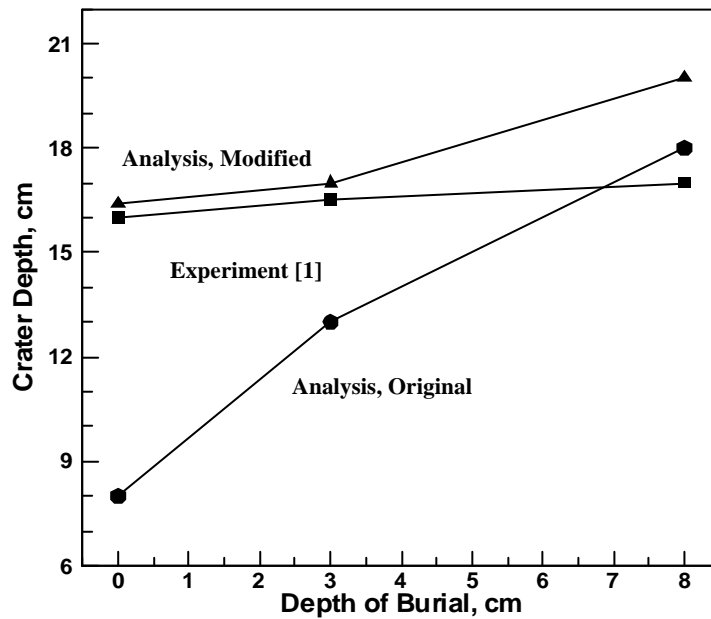
Fig.17. Variation of the crater depth with the charge depth
of burial. Please see text for details.
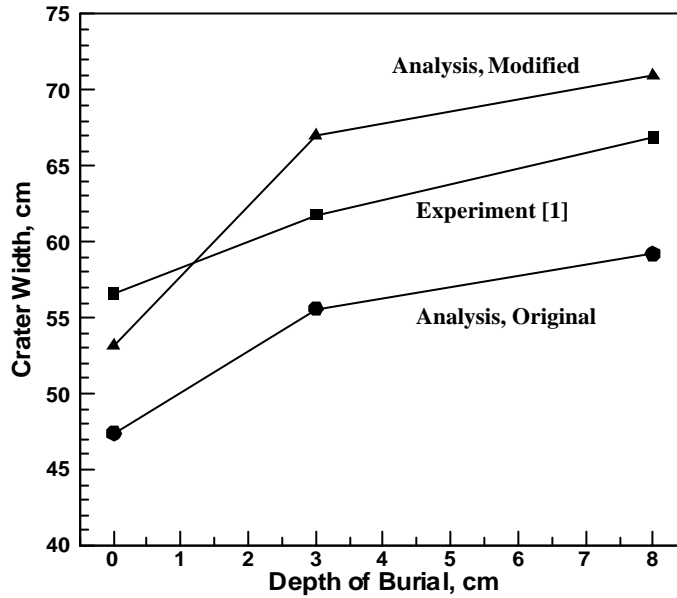
Fig.18. Variation of the crater width with the charge depth of burial.
Please see text for details.

4. CONCLUSIONS

Based on the results obtained in the present work, the following main conclusions can be drawn:

1. A purely Eulerian multi-material approach to the computational analysis of the detonation phenomena associated with shallow-buried mines in sand appears to provide realistic predictions regarding various early post-detonation phenomena such as the formation of sand bubbles, detonation product clouds, compression waves in sand and shock waves in air.

2. At the later stages of the detonation the computational results are not in as good agreement with their experimental counterparts, in particular, with respect to the shape and size of sand craters. These discrepancies are attributed to the potential shortcomings of the materials model for sand.

3. Late stage post-detonation phenomena such as the sand crater size and shape are found to be fairly sensitive functions of the sand's material constitutive model. Hence, a good agreement between a computational and experimental model for a shallow-buried mine can be expected only if reliable material constitutive models are available.

ACKNOWLEDGEMENTS

REFERENCES

[1]. D. Bergeron, R. Walker and C. Coffey. *Detonation of 100-gram Anti-Personnel Mine Surrogate Charges in Sand-A Test Case For Computer Code Validation*. Suffield Report No. 668, Defense Research Establishment Suffield, Ralston, Alberta, Canada, April 1998.

[2]. *AUTODYN-2D and 3D, Version 5.0, User Documentation*. Century Dynamics Inc., 2004.

[3]. M. P. Braid and D. Bergeron. *Experimental Investigation and Analysis of the Effects of Anti-Personnel Landmine Blasts*. DRES SSP 2001-188, Defense Suffield Publication, Canada, December 2001.

[4]. G. Fairlie and D. Bergeron. Numerical Simulation of Mine Blast Loading on Structures. *17th Military Aspects of Blast Symposium*, Las Vegas, Nevada, June 2002.

[5]. O. A. Artyunov, S. S. Grigoryan and R. Z. Kamalyan. Effect of Soil Moisture Content on Parameters of Crater Cuts. *Combustion Explosion and Shock Waves*.21 (1985)259-262.

[6]. B. K. Hodge and Keith Koenig. *Compressible Fluid Dynamics*. Prentice Hall, Englewood Cliffs, New Jersey, 1995.

[7]. E. L. Lee, H. C. Hornig and J. W. Kury. *Adiabatic Expansion of High Explosive Detonation Products*. UCRL-50422, Lawrence Radiation Laboratory, University of California, 1968.

[8]. P. W. Cooper. *Explosives Engineering*. Wiley-VCH, New York, 1996.
[9]. J. F. Moxnes, G. Odegardstuen, A. Atwood and P. Curran. Mechanical Properties of a Porous Material Studied In a High Speed Piston Driven Compaction Experiment. *30th International Annual Conference of ICT*, Karlsruhe, Federal Republic of Germany, June 29-July 2, 1999.

[10]. L. Laine and A. Sandvik. Derivation of Mechanical Properties for Sand. *Proceedings of the 4th Asia-Pacific Conference on Shock and Impact Loads on Structures*, CI-Premier PTE LTD, Singapore, November 2001, 361-368.